INTERNATIONAL JOURNAL OF HYDROGEN ENERGY 40 (2015) 10908–10917

Available online at www.sciencedirect.com

ScienceDirect

journal homepage: www.elsevier.com/locate/he

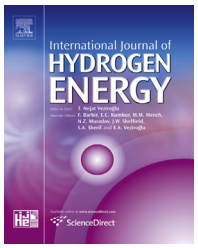

From determination of the fugacity coefficients to estimation of hydrogen storage capacity: A convenient theoretical method

Peng Fu [a], *Ran Jia* [a,*], *Chui-Peng Kong* [a], *Roberts I. Eglitis* [b], *Hong-Xing Zhang* [a,*]

[a] *Institute of Theoretical Chemistry, Jilin University, 130023 Changchun, PR China*
[b] *Institute of Solid State Physics, University of Latvia, 8 Kengaraga Str., Riga LV1067, Latvia*

ARTICLE INFO

Article history:
Received 15 April 2015
Received in revised form
31 May 2015
Accepted 3 July 2015
Available online 22 July 2015

Keywords:
Equation of state
Virial expansion
DFT
Density profile

ABSTRACT

The equation of state (EOS) from virial expansion (VE) is used in this work to pave the way for determining the fugacity coefficients of the hydrogen fluid at arbitrary temperature and pressure. The fugacity coefficients from our VE method have more physical meanings than the empirical values. In this way, the hydrogen storage capacity of a novel material model can be estimated by using few density functional theory (DFT) calculations with the aid of a continuum model. The efficient continuum model can provide a more accurate estimation of the hydrogen storage capacity than the pure DFT calculations. Furthermore, the expensive grand canonical ensemble (μNT) simulations combining with the quantum mechanics methods (i.e., QM/MD-μNT) are unnecessary within this method. The hydrogen fluid can be handled with our VE method at the temperature in the range of 160–773 K. The hydrogen storage capacity and the detailed thermodynamic information of a designed novel material can thereby be estimated by using this method with relatively high accuracy and low computing cost. As an example, the hydrogen storage capacities of the expanded bilayer graphene systems are presented. Our theoretical results agree with the experimental values very well.

Introduction

Our daily life depends on various energy sources. Hydrogen is an ideal "green" energy resource on account of its high efficiency and environmental friendliness. However, the compact storage and safe delivery of the hydrogen fluid are the main challenges for its application. The emphasis is to design novel hydrogen storage materials which can satisfy the gravimetric density of hydrogen more than 5.5 *wt.*% and 0.04 g/cm^3 at ambient temperature and pressure by the year 2015 targeted by the U.S. Department of Energy. In addition, the hydrogen storage materials should also be able to desorb the hydrogen molecule under ambient thermodynamic conditions. Therefore, the hydrogen adsorption energy is required to lie between the physisorbed and chemisorbed states, i.e., around 0.1–0.3 *eV* per H_2 [1–3]. In practical applications, for example,

* *Corresponding authors.*
E-mail addresses: jiaran@jlu.edu.cn (R. Jia), zhanghx@jlu.edu.cn (H.-X. Zhang).
http://dx.doi.org/10.1016/j.ijhydene.2015.07.005

to fuel a typical automobile, the system is required to contain at least 7.5 *wt.*% and 0.07 g/cm^3 hydrogen fluid at a minimum temperature of 243 *K* and a maximum pressure of 10 *MPa* [4]. Therefore, the studies at too low temperatures or too high pressures are not practical. This is also the reason why we limit our study in a certain temperature and pressure range in this work. Because of the large surface area and light weight, the carbon and boron nitride materials have been extensively studied for hydrogen adsorption [5–12]. According to previous studies, the perfect single layer graphene do not have high hydrogen storage capability. However, the simple and high symmetric structure of the graphene system is indeed a perfect model to validate our method for predicting the hydrogen storage capability.

To study the surface properties and the adsorption process of a hydrogen storage system, various methods, including DFT, quantum mechanics combining with molecular dynamics (QM/MD) and classical molecular dynamics with force field, have been used in the research works. In particularly, all of these methods have some kind of deficiencies. The pure DFT calculation has been employed to predict the hydrogen storage capacity for the novel material system over years. One can add the hydrogen molecule into the system one by one, until the total adsorption energies close to zero or even positive. This strategy depends on the full geometry optimization for each hydrogen adding step. To get an rational results of hydrogen-surface interaction, the local density approximation (LDA) or the generalized gradient approximations (GGA) plus a long-range dispersion correction (e.g., suggested by Grimme [13], by Tkatchenko and Scheffler [14], or by Ortmann, Bechstedt and Schmidt [15]) have been used. Actually, the LDA cannot provide the expected r^{-6} London dispersion interactions resulting in the lack of reliability for the predicted hydrogen storage capacity. A reasonable distance between the adsorbate and adsorbent cannot be obtained from the pure GGA simulation. Unfortunately, even with the help of a dispersion correction, the hydrogen storage uptake rate predicted from DFT calculation is almost always overestimated due to the missing of the thermodynamic part. The QM/MD method, e.g., Car-Parrinello molecular dynamics [16], which looks like a good way to obtain the accurate estimation with full thermodynamic information, is still expensive and time-consuming for a μNT simulation. The classical force field molecular dynamics simulation can rapidly provide an acceptable prediction result. But an adequate force field has to be assigned.

In order to balance the simulation speed and accuracy, Morris' group suggested using the feature of the chemical potentials in the equilibrium state between the in- and outside phases to get the density distribution profile of the adsorbed hydrogen fluid in the storage material system [17–20]. Their researches were following the works of Patchkovskii [21] and Cabria [22]. With this efficient continuum model, one can estimate the hydrogen uptake rate by calculating the adsorption energies of single hydrogen molecule at several positions in the material system. The dynamic simulation and the simulation with complicated configurations of the full hydrogen fluid in the material are not necessary any more. The thermodynamic information and the intermolecular interactions between the H_2 molecules should be contained in the fugacities of the gaseous and adsorbed states. It is brilliant to connect the quantum mechanical simulation directly with the statistical mechanics. However, Morris' group set the fugacity coefficients in their works [17–19] either to the unity, or to an empirical value fitted by Shaw and Wones [23] in 1964. Obviously, the fugacity coefficients could be totally different, especially at low temperature. Although the empirical value for the hydrogen fluid in their work [19] seems to be close to the experiment, the old fitting process is not reliable. Thus, we conclude four points which should be considered: i). The numerical calculation ability was very low at half a century ago. Moreover, this formula was obtained by fitting the "linear portions" of the experimental curves "by eye" [23]; ii). The experimental technique before 1964 is very limited, e.g., the temperature and pressure control techniques. One cannot totally trust such outdated experimental results, which are precisely the basic data of this empirical formula; iii). This empirical expression applies only to the hydrogen gas, and only from 273 to 1273 *K*. For other non-polar particle fluids or at a temperature below 273 *K*, this formula is no longer applicable; iv). This empirical formula has less physical meanings. On the other hand, one also need an expression for the EOS of the hydrogen fluid. The empirical expression for the hydrogen EOS used in Morris' works [17–19] was introduced by Mills et al. [24] in 1977, which applies only for hydrogen fluid at high pressure from 200 to 2000 *MPa*. Analogously, this formula is fitted on the basis of a polynomial model and has less physical meanings. Very recently, Morris' group presented their predictions of the uptake rates of the methane in nanoporous carbons [20]. In that work, the EOS fitted by Setzmann and Wagner [25] was used to determine the fugacity coefficients of the methane. It is worth noting that these EOSs cannot be directly transplanted into the calculations for the other species.

The uptake rates of the hydrogen and methane fluids in the nanoporous carbons predicted by Morris' group [19,20] with suitable fugacity coefficients show the acceptable accuracy with this strategy. The predicted results are around 20% less than the experiments. Considering the variability of the experimental pore morphology and the uncertainty of the measurements, these theoretical estimations agree with the experiment fairly well. The combination of the effective continuum model and the DFT calculations (with van der Waals correction terms) is an inexpensive and accurate approach for rational design of novel physisorption-based gas storage materials. In order to fill the only flaw of this method, which is just the empirical expressions of the fugacity coefficients and the EOS, we are spurred to find a way for determining the fugacity coefficients with full physical meanings. With the rapid development of computing ability, one can already numerically determine the EOSs for some simple fluids with assistance of certain intermolecular potential models. The Lennard-Jones (LJ) potential is very simple and common. But it is well-known that the quantum effects are remarkable for the hydrogen fluid at low temperature. Therefore, a quantum correction term is necessary for the LJ potential, which is named as Feynman-Hibbs (FH) potential model. Based on such potential models, we can write the EOS as a VE form. This expression for the EOS now has full physical meanings. The LJ and FH models describe only the additive particle–particle

interaction. For a dense fluid, the high order many-body interaction model is needed. However, as we will show in the text, the three-particle interaction can already be neglected if the temperature of the hydrogen fluid is above 200 K which is already lower than the minimum temperature in the practical applications. Another advantage is that the other non-polar fluids can also be treated by using this method. After that, the results can be directly used in the Morris' strategy [17–20] to assess the gas storage capacity of a novel material system. The details will be discussed in the main text. Using the hydrogen fugacity coefficients determined with our VE method, we reassess the hydrogen storage capacities of the expanded bilayer graphene systems with the aid of the continuum model and our EOS. Our estimated hydrogen storage capacities are close to the experimental results and more accurate than Morris' predictions.

This work is organized as follows: In section Theoretical estimation of the fugacity coefficient, the determination process for the fugacity coefficients of a non-polar particle fluid by using our virial expansion method is clearly explained. The hydrogen fluid is employed as an example; In section Prediction of the hydrogen uptake rates, we present how to use the calculated fugacity coefficients in conjunction with our EOS to obtain the pressure profile of the hydrogen storage material. Whereby, the hydrogen density profile and assess the hydrogen uptake rates of the storage material systems can be figured out with the help of a simple integration. Different interlayer spacings of the bilayer graphene sheets are also considered in this section; A short conclusion is given in section Conclusion.

Theoretical estimation of the fugacity coefficient

In a gas storage material system, the chemical potentials between the system and the environment should be equal when reaching the equilibrium state. The fugacity of a real gas can replace the mechanical pressure to describe the chemical thermodynamic process as the role of an effective pressure. The fugacity is defined based on the so-called fugacity coefficient ϕ:

$$f = \phi P, \tag{1}$$

where P is the true mechanical pressure. For an ideal gas, the fugacity coefficient ϕ is unity. Thus, the fugacity and pressure are equal to each other. The fugacity coefficient can be fixed by using Eq. (2) at particular T and P. V_m in Eq. (2) denotes the molar volume of the real gas, and R is the Avogadro constant.

$$\ln \phi(T,P) = \frac{1}{RT}\int_0^P \left(V_m(P') - \frac{RT}{P'}\right) dP' \tag{2}$$

In Eq. (2), the $RT\ln\phi(T,P)$ represents the contribution of non-ideality to the chemical potential of the real gas.

V_m is the only uncertain quantity in Eq. (2). For a real system, it is not very easy to give out an EOS. Therefore, the VE form is used to describe the EOS for a real system:

$$\frac{PV_m}{RT} = 1 + \frac{B(T)}{V_m} + \frac{C(T)}{V_m^2} + \frac{D(T)}{V_m^3} + \cdots, \tag{3}$$

where the $B(T)$, $C(T)$ and $D(T)$ are the second, third and fourth virial coefficients, respectively. The expansion is an infinite series. $B(T)$ term describes the two-body interactions, $C(T)$ term describes the three-body interactions, and so on. Even though the terms above the third virial coefficient are rarely used in chemical thermodynamics, our study still includes the contributions until the fourth virial term to get the accurate fugacity coefficients compared with the experimental values. But the molar volume in Eq. (3) cannot be solved easily. Fortunately, we can rewrite the VE for the EOS in powers of the pressure:

$$\frac{PV_m}{RT} = 1 + B'(T)P + C'(T)P^2 + D'(T)P^3 + \cdots. \tag{4}$$

The new virial coefficients B', C' and D' can be fixed via equating the coefficients of V_m^{-1}, V_m^{-2} and V_m^{-3} in Eqs. (3) and (4). That gives:

$$B'(T) = \frac{B(T)}{RT}, \tag{5}$$

$$C'(T) = \frac{C(T) - B^2(T)}{R^2T^2}, \tag{6}$$

$$D'(T) = \frac{D(T) - 3B(T)C(T) + 2B^3(T)}{R^3T^3}. \tag{7}$$

To calculate the virial coefficients, a suitable formula is needed to describe the particle–particle interaction. The most popular and simple model is the LJ-potential:

$$U_{LJ}(r) = 4\varepsilon\left[\left(\frac{\sigma}{r}\right)^{12} - \left(\frac{\sigma}{r}\right)^{6}\right]. \tag{8}$$

However, the LJ-potential cannot describe the second virial coefficient of the hydrogen fluid very well at low temperature [26]. Therefore, A quantum correction for LJ-potential is necessary. Feynman and Hibbs suggested an Gaussian type effective potential (i.e., FH-effective potential) based on the LJ-potential [27]. The Taylor expansion until second order for this FH-effective potential [28] is employed in this work:

$$U_{LJ}^{FH}(r) = U_{LJ}(r) + \frac{\beta\hbar^2}{24m_r}\left(\frac{d^2}{dr^2} + \frac{2}{r}\frac{d}{dr}\right)U_{LJ}(r), \tag{9}$$

where β denotes the inverse of k_BT, and m_r is the reduced mass of the LJ pairs. We focus on the hydrogen fluid in this work. Thus, m_r is equal to 1.6744×10^{-27} kg [29]. Note that the diatomic hydrogen molecule is treated here as an entity. The other parameters for the LJ-potential are set to $\varepsilon = 3.160$ meV and $\sigma = 2.958$ Å for hydrogen molecules [29–32]. The critical point of the normal hydrogen fluid is located at $T = 33.145$ K, $P = 1.296$ MPa and $\rho = 0.0313$ g/cm^3 [33]. Its liquid density at boiling point (i.e., $T = 20.369$ K and $P = 101.325$ kPa) is 0.07085 g/cm^3 [33].

There exist two different spin isomers of the diatomic hydrogen molecules: parahydrogen and orthohydrogen. The parahydrogen has two antiparallel proton spins to form a singlet state. The orthohydrogen has conversely two parallel aligned proton spins, wherefore a triplet state is formed. At the ambient temperature and pressure, the hydrogen gas is known as the normal hydrogen which contains about 25% of the parahydrogen and 75% of the orthohydrogen. All of our

calculations are under the assumption that the hydrogen fluid retains the normal form. Although the ratio of the spin isomers depends on the temperature, the operating temperature range for a hydrogen storage material is not very wide, and the effect of the ratio change can be covered in the estimation errors.

Second virial coefficient

The calculation of the second virial coefficient $B(T)$ is a matter of common knowledge in the literature [34,35]. The second virial coefficient for a two-body potential model is given by

$$B(T) = -2\pi \int_0^\infty r^2 f_{12} dr, \tag{10}$$

with a Mayer-f function:

$$f_{ij} = \exp\left[-\beta U(r_{ij})\right] - 1, \tag{11}$$

where $U(r_{ij})$ describes the two-body potential and its subscripts i and j are the labels of two particles. $B(T)$ corresponds to interactions of the molecule pairs.

Harvey and his coworkers [36,37] presented their calculated second virial coefficients for molecular hydrogen H_2, deuterium D_2, and tritium T_2, along with the mixed its isotopologues by using Path-integral Monte Carlo (PIMC) method with the high-accuracy four- and six-dimensional (4D and 6D) potential energy surfaces. Additionally, they used the semiclassical calculation with the 4D potential energy surface, and the fully quantum computation for normal hydrogen from the isotropic approximation to the 4D potential. To compare our potential energy model with Harvey's, we plot the results of the calculated $B(T)$ in the top panel of Fig. 1. The solid and dashed lines represent the results with the FH-effective potential and simple LJ-potential, respectively. The symbols show the results from Harvey's group [36,37]. As we can see, there is no obvious different among all methods at high temperature, i.e., $T \geq 200$ K. The FH-effective potential model can describe the behavior of $B(T)$ very well at very low temperature, even under the critical temperature of the normal hydrogen fluid. The LJ-potential model, however, provides a relatively large deviation at the temperature lower than 100 K. This deviation points out the quantum effect of the hydrogen molecule at low temperature. The estimated fugacity coefficients ϕ(273 K,P) using Eqs. (2), (4) and (5) including our calculated $B(T)$ are plotted in the bottom panel of Fig. 1. The circles represent the results for the empirical formula proposed by Shaw and Wones [23]. Although the $B(T)$ from FH-model still provides a large deviation compared with the empirical data, the results from FH-model are much better than those from simple LJ-potential.

Third virial coefficient

Because of the large inaccuracy of the estimated fugacity coefficients by only using $B(T)$, the next order of the virial expansion has to be considered. In the virial expansion form, the third term represents the effect from the three-body interaction. In other words, there is also non-additive

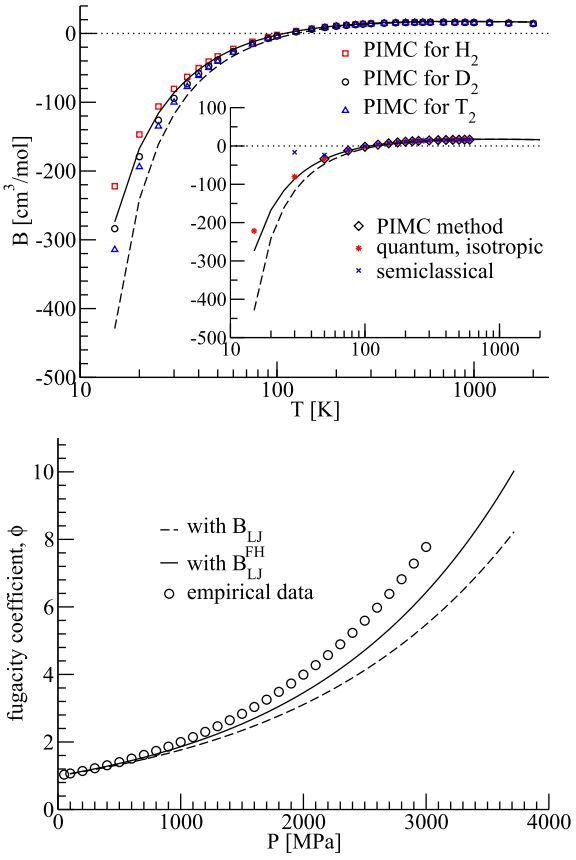

Fig. 1 – Top panel: the second virial coefficient $B(T)$ of the hydrogen fluid as a function of the temperature. Dashed lines are obtained from the LJ-potential; solid lines denote the results from FH-effective potential; symbols are calculated by using different methods with 4D/6D potential-energy surfaces [36,37]. Bottom panel: the fugacity coefficient ϕ at $T = 273$ K as a function of the pressure. The circles are from the empirical formula [23]; the lines describe our calculation results related to the $B(T)$. Dashed line is obtained from $B_{LJ}(273)$; solid line is from the calculation with help of $B_{LJ}^{FH}(273)$.

interaction besides the pairwise additive interaction energy. Therefore, the $C(T)$ can be divided into two parts:

$$C(T) = C_{add} + \Delta C, \tag{12}$$

where C_{add} denotes the contribution due to the pairwise additive potential, namely FH- or LJ-potential in this work. ΔC arises due to the non-additive three-body potential. More details about the definition of ΔC can be found in Ref. [38]. The related energy difference between the two- and three-body potential is given by

$$\Delta U_{ijk} = U_{ijk} - \left(U_{ij} + U_{ik} + U_{jk}\right). \tag{13}$$

Because of the difficulty for numerically solving the two-body term of $C(T)$, we assume $U_{ijk} = 0$, and obtain the simplified form with $\Delta C = 0$. The form for the third Viral coefficient can therefore be expressed as (see Ref. [38] for details)

$$C(T) = -16\pi^2 \int_0^{\infty} f_{ij} r_{ij} \int_{r_{ij}/2}^{r_{ij}} f_{ik} r_{ik} \int_{r_{ij}-r_{ik}}^{r_{ik}} f_{jk} r_{jk} dr_{jk} dr_{ik} dr_{ij}. \quad (14)$$

The results from our approximation and the other works are plotted in the top panel of Fig. 2. The LJ-potential shows a large deviation, especially in the low temperature region. The performance of our FH-model at low temperature region (i.e., $T < 200$ K) is not fully satisfactory, either. Fortunately, the functional temperature range for a hydrogen storage material system is expected to be located above 200 K. In the range from 200 to 1000 K, the results from our FH-model agree fairly well with the results suggested by Garberoglio [39] for para-hydrogen. The deviation is lower than 10%. In details, Garberoglio worked with PIMC calculations, which were performed in conjunction with the three-body interactions suggested by Axilrod, Teller, Muto [40,41] (ATM) and Manzhos et al. [42]. Even though we can only find these data for para-hydrogen fluid, we believe that the comparisons with our results for normal hydrogen fluid are still meaningful. Not only the calculations by using our models but also those by PIMC method with only two-body potential show the same conclusion, that the non-additive three-body potential at high temperature provides almost no contribution to the third virial coefficients, if we compare them with the results considering the three-body term. It means further more that our assumption about $U_{ijk} = 0$ at temperature $T > 200$ K for the H_2 fluid is reasonable and suitable. It is worth to note that again, the purpose of this method is to find a way to estimate the theoretical values of the fugacity coefficients and the EOS of the hydrogen fluid under the condition of $T \geq 243$ K in a practical hydrogen storage system. On this premise, the non-additive three-body potential and even higher order potentials can be ignored because of the above discussion.

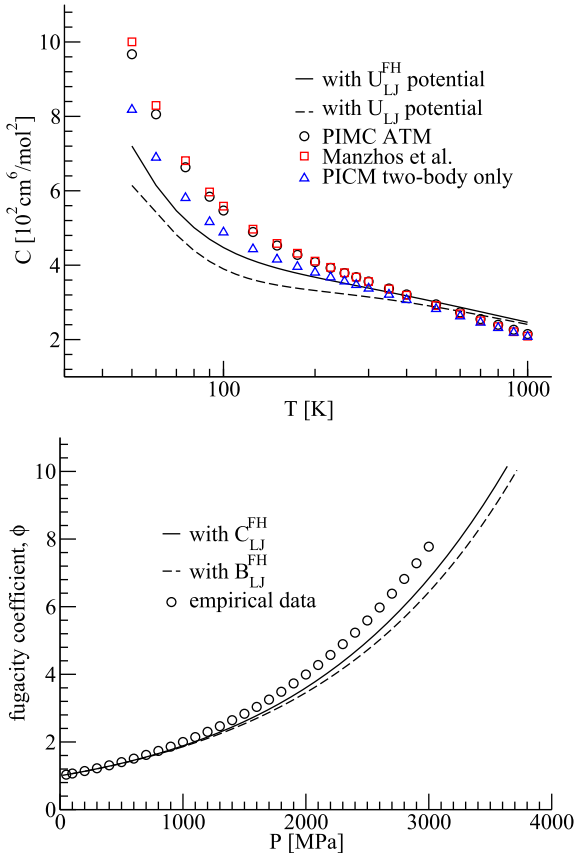

Fig. 2 – Top panel: the third virial coefficients $C(T)$ of hydrogen fluid as a function of the temperature. Doted lines are obtained from the LJ-potential for normal hydrogen fluid; solid lines denote the results from FH-effective potential for normal hydrogen fluid; symbols are calculated for parahydrogen fluid by using PIMC method with two different three-body interactions (ATM and Manzhos) and even two-body interaction by Garberoglio [39]. Bottom panel: the fugacity coefficient ϕ at $T = 273$ K as a function of the pressure. The circles are from the empirical formula [23]; Dashed line is obtained by using $B_{LJ}^{FH}(273)$; solid line is from the calculation with help of $B_{LJ}^{FH}(273)$ and $C_{LJ}^{FH}(273)$, together.

Comparing with the calculated fugacity coefficients from $B(T)$, the combination of $B(T)$ and $C(T)$ can provides better results, especially in high pressure region (as shown in the bottom panel of Fig. 2). But, the current theoretical estimation is still far away from the empirical points after 2000 MPa. Hence an improving accuracy motivates us to try the higher order of the VE to obtain a set of satisfactory results.

Fourth virial coefficient

The fourth virial term is important only when the fluid is very dense. As we conclude above, the non-additive three-body interaction can already be neglected at the temperature $T > 200$ K. Therefore, the non-additive four-body interaction will also not be considered here. The numerical calculation for $D(T)$ even with the simple LJ-potential model is a very complicated and tedious mission. The LJ-potential has an attractive term and a repulsive term to represent the potential energy between two particles. The attractive term will be important when the distance between the particles is larger than the balance distance. Conversely, when the distance is shorter than the balance one, the repulsive term will play the major role. In fact, our researched fluid is already dense enough, so that the repulsive term is the major contribution, and the attractive term can be discarded in this situation. Without an attractive term, the LJ-potential degenerates into a soft-sphere potential model. From this point, one can easily obtain the fourth virial coefficient with the help of the reduced one, $\tilde{D}$. An asymptotically consistent approximate method is employed:

$$D(T) = \tilde{D}\left[\sigma(\beta\varepsilon)^{\frac{1}{n}}\right]^9, \quad (15)$$

which is introduced by Barlow, Schultz, Weinstein and Kofke [43], recently. The reduced virial coefficient $\tilde{D}$ is a function only of n and is known from the literature [44–46]. The parameter n characterizes the hardness of the particles. When $n \to \infty$, the soft-sphere model degenerates again into the hard-sphere model. Note that for the small n (i.e., softer potentials), the non-monotonic coefficients can lead to a poorly converging virial series, as emphasized by Wheatley [44]. For this reason, we choose $n = 24$ here, and then the $\tilde{D} = 3.18751$

can be found from the work by Wheatley [44]. Using Eq. (15), we plot the fourth virial coefficients for a soft-sphere model with $n = 24$ as a function of temperature in Fig. 3.

As shown in Fig. 4, the VE up to the fourth term can already describe the fugacity coefficients (top panel) and the states of the hydrogen gas (bottom panel), very well in ranges of the hydrogen storage conditions. Since the empirical expression [23] applies from 273 *K* to 1273 *K*, only the fugacity coefficients at 273 *K*, 373 *K* and 773 *K* are plotted in the top panel of Fig. 4. As shown in the bottom panel of Fig. 4, our estimated isotherm at 100 *K* deviates from the reference values [24,47] under high pressure. The reason could be the ratio of the spin isomers. Anyhow, this temperature is far lower than the application temperature for the hydrogen storage materials. The isotherm at $T = 160$ *K* agrees with the references [24,47] very well. Thus, the rest higher order terms in the VE form can be abandoned. The deviations at $T = 273$ *K* between our method and the empirical formula are all smaller than 6.2% up to 3000 *MPa*. The accuracy of our VE method is therefore acceptable. The calculated fugacity coefficients with our VE method can be trusted for the hydrogen fluid, in range of temperatures from 160 *K* to 773 *K* and pressures from 1 *MPa* to 2000 *MPa*.

Prediction of the hydrogen uptake rates

The determination process for the fugacity coefficients and the EOS of the hydrogen fluid, as an example, has been discussed above clearly. We also must emphasize that our method has a very accessible form and a wide applicability. It could be used not only for hydrogen fluid but also for the other non-polar particle fluids with suitable interaction parameters. The expanded bilayer graphene sheets are employed in this work as the example material system because of their simplicity and high symmetry of the structures. The hydrogen storage system could be considered as a continuum model. At equilibrium, the chemical potentials in the adsorbed phase and free gaseous phase (in other words, in- and outside of the material system) should also be the same. Therefore, the

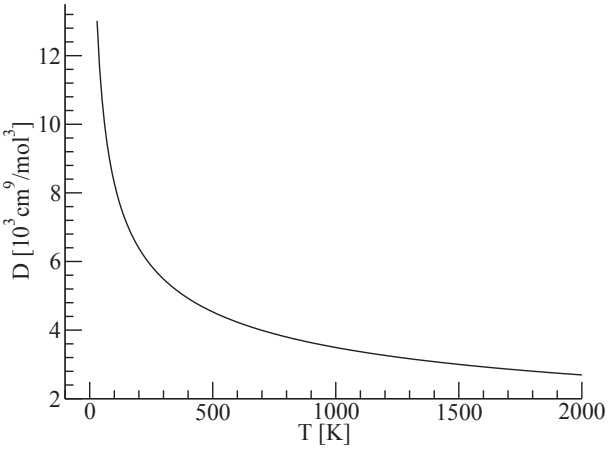

Fig. 3 – The fourth Virial coefficient $D_{ss}(T)$ of the normal hydrogen fluid determined by using a soft-sphere potential from Eq. (15) with $n = 24$.

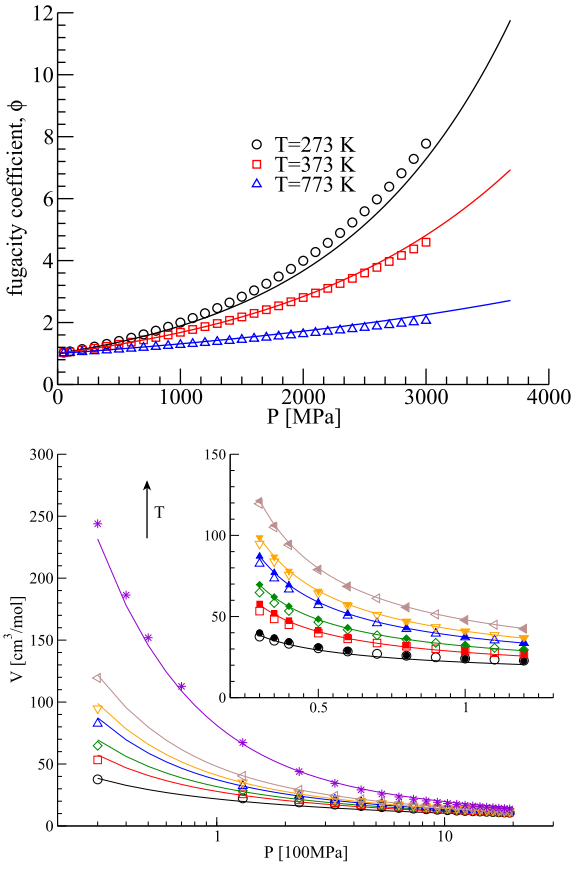

Fig. 4 – Top panel: fugacity coefficient as a function of pressure at three different temperatures: 273 *K* (black), 373 *K* (ret) and 773 *K* (blue); lines are calculated by using our theory; symbols are from the empirical function [23]. Bottom panel: the *PV* diagram for the normal hydrogen fluid at the temperatures $T = 100$ *K* (black), 160 *K* (red), 200 *K* (green), 260 *K* (blue), 300 *K* (orange), 380 *K* (brown) and 773 *K* (violet) from bottom to top, respectively; lines are calculated by using our EOS; hollow symbols are from the empirical formula suggested by Mills et al. [24]; filled symbols represent the data for parahydrogen introduced in the work by Younglove [47]. The x-axis of the *PV* diagram is on the logarithmic scale, whereas the x-axis of the inset is normal. (For interpretation of the references to color in this figure legend, the reader is referred to the web version of this article.)

adsorption energy of a hydrogen molecule in this material system, which is calculated by using quantum mechanical method, can be introduced in the calculation as follows:

$$P_{in} = \frac{\phi_{ext}}{\phi_{in}} P_{ext} \exp\left[-\beta E_{in}^{ads}\right], \tag{16}$$

where E_{in}^{ads} represents the adsorption energy of a single hydrogen molecule inside of the storage system. The validation of the assumption that this thermodynamic expression in Eq. (16) is accurate for the calculation of hydrogen uptake in carbon slit pores, has been proved very carefully by using Grand canonical Monte Carlo simulations in the work by Peng and Morris [17]. In fact, the hydrogen storage capacities of the

nanoporous carbons and the expanded bilayer graphene with a series of the interlayer distances have already been reported with the similar strategy, but under the assumption that the fugacity coefficient is equal to unity or a empirical value [17,19,20]. It is of course not very precise. Thus, we re-assess the hydrogen uptake rates of the artificially expanded bilayer graphene sheets with four different interlayer spacings of 6, 7, 8 and 9 Å to inspect the applicability of our VE method and the whole strategy for the prediction of the hydrogen uptake rates.

Adsorption energy calculations

To determine the pressure and the related fugacity coefficient for the inside phase, the only unknown in Eq. (16) is the adsorption energy E_{in}^{ads}. The adsorption energy can be defined as follows:

$$E_{in}^{ads} = E_{tot}(X + H_2) - E_{tot}(X) - E_{free}(H_2), \quad (17)$$

where X denotes the hydrogen storage system, and $E_{tot}(X)$ represents the total energy of the material system, $E_{free}(H_2)$ points out the energy of a free hydrogen molecule, $E_{tot}(X+H_2)$ is the total energy of the material system X with an adsorbed hydrogen molecule at certain position. All of the energy quantities can be calculated by using DFT methods. In this work, the calculations for the energy quantities are performed by the CRYSTAL14 computer code [48], which employs Gaussian-type functions localized at the atoms as basis for an expansion of the crystalline orbitals. The all electron Gaussian basis sets of triple-zeta valence with polarization quality (TZVP) are applied, which are developed for carbon and hydrogen atoms by Peintinger et al. [49]. A 3×3 supercell is created in ab-plane for the expanded bilayer graphene system. The reciprocal space integrations are performed by sampling the two-dimensional Brillouin zone of the supercell with 96×96 Pack-Monkhorst net [50]. To get a reasonable adsorption energy, the semi-empirical dispersion correction term suggested by Grimme [13] is also employed in our calculations. The dispersion coefficient C_6 is set to 1.75 $J \cdot nm^6 \cdot mol^{-1}$ for the carbon atom as suggested in the original work by Grimme [13]. The atomic van der Waals (vdW) radius of the carbon atom R_0 is set to 2.21 Å to get a reasonable interlayer distance of the graphite. The parameters C_6 and R_0 for the hydrogen atom are set to 0.14 $J \cdot nm^6 \cdot mol^{-1}$ and 1.20 Å, respectively. The calculations are performed with B3LYP-D2. The thresholds N (i.e., the accuracy of the integrals 10^{-N}) in our calculations are set as 8, 8, 8, 8 and 16 for the Coulomb overlap, Coulomb penetration, exchange overlap, the first- and second-exchange pseudo-overlaps, respectively. The lattice parameters of the graphite are $a = 2.450$ Å and $c = 6.500$ Å after the full geometry optimizations within B3LYP-D2. The geometric structure of the graphite from B3LYP-D2 is acceptable with the maximum deviations less than 4% compared with the experimental results $a = 2.464$ Å and $c = 6.711$ Å [51]. Considering the large interlayer distances of our object systems (i.e., 6, 7, 8 and 9 Å sheets separations), we chose the same lattice constant of the single layer graphene (2.451 Å within B3LYP-D2) as the in-plane lattice constant for our bilayer graphene calculations. The thickness of the vacuum layer is set as $c = 500$ Å to avoid the unexpected interaction from the periodic neighbors. Not only to simplify the prediction process, but also due to the slight long-range dispersion interactions for the very large interlayer spacing, the graphene sheets in our simulations are aligned as hexagonal (AA) stacking arrangement along the c-axis.

Hydrogen uptake rates

There is difference between the adsorbed and free hydrogen molecules. However, the difference is very small owing to the essence of the physical adsorption. Through our calculations, the largest deviation of the Mulliken charges of the hydrogen atoms between the adsorbed and free hydrogen molecules is only 5.3%, in the effective adsorption regions between the graphene sheets. This deviation could be covered by the system errors. Therefore, it is acceptable that the ideal hydrogen model is employed throughout the calculations. More details can be found in the Support Information. The DFT single point calculations are following the schema introduced in the work by Ihm [19]. The adsorption energy is sampled along the c-axis between two graphene layers. The distributions of the electron and the electrostatic potential on the graphene are heterogeneous. Therefore, the hydrogen adsorption energy could not be uniform in the fixed plane. According to our preliminary calculations, the lowest adsorption energy can be obtained just above the center position of the six-ring for a certain height, whereas the highest adsorption energy is above the carbon atoms. Fortunately, the symmetry of the carbon six-ring is very high. One can get the distribution map of the adsorption energy with assistance from the symmetry. As shown in Fig. 2 in Ref. [19], the energy differences in a plane with a fixed c-axis coordinate are not very significant in the main region. Thus, only the center point in the six-ring is considered in the sampling of this work. Note that this simplify is rough, of course. However, our purpose is to test the feasibility of our VE method by estimating the hydrogen storage capacities. Our pre-calculations indicate also that the vertical hydrogen molecule to the graphene surface has the lower energy than the parallel hydrogen molecule. The difference between them is actually very tiny in the region with major contributions. On this point, the Support file of the work by Ihm [19] can also be used as reference. Therefore, as a quick test, the energy difference caused by the orientation of the hydrogen molecule is also neglected.

In Fig. 5, the profiles of the adsorption energies (in top panel) and the uptake rates (in bottom panel) for four bilayer graphene systems are presented. The circles, squares, diamonds and triangles indicate the value for the systems with the interlayer distances of 6, 7, 8 and 9 Å, respectively. The general shapes of the profiles are similar to Fig. 3 in the work by Ihm et al. [19]. But the double well potential starts to develop already at the interlayer distance of 8 Å. This is caused by the different treatments of the dispersion interactions between the hydrogen molecule and the carbon atoms introduced by Grimme [13] and Ihm [19]. This indicates that the calculation method for the determination of the adsorption energy should be chosen very

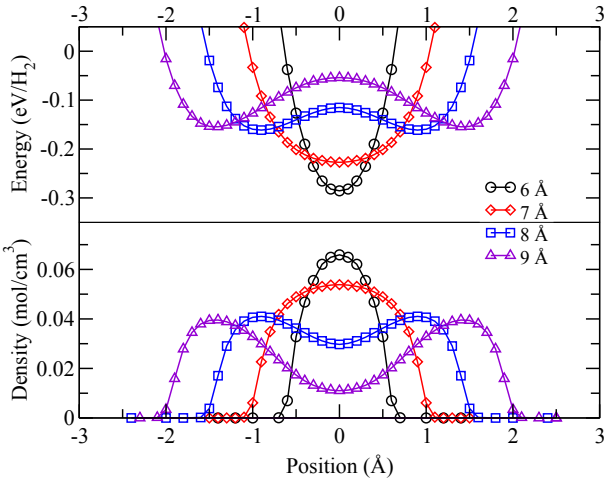

Fig. 5 – The adsorption energy (top panel) and hydrogen density (bottom panel) profiles in the bilayer graphene systems with 6 Å (circles), 7 Å (diamonds), 8 Å (squares) and 9 Å (triangles) interlayer spacings at the temperatures 298 *K* and the pressure 5 *MPa* calculated by using B3LYP-D2. The positions are sampled along the c-axis, and the zero position is defined in the middle of two graphene layers.

carefully, before the research is indeed carried out. Different methods for the adsorption energy calculation can bring more than 30% departures into the final results. Fig. 6 depicts the varieties of the hydrogen uptake rates in four bilayer graphene systems as the pressure rise. The symbols have the same meaning as shown in Fig. 5. The solid, patterned and hollow symbols denote the uptake rates at $T = 298, 273, 243$ *K*, respectively. The hydrogen uptake rate increases slower as the pressure rise in the relatively large pressure region (i.e., $P > 5$ *MPa*). As shown in Fig. 6 (more clearly in the inset) the uptake rate increases in the large pressure region with the increasing interlayer distance, but the variation decreases. This means that the expanded bilayer graphene sheets system possesses an ultimate value for the hydrogen storage capacity. The adsorbance of the 9 Å separation exceeds it in the 8 Å system after around 3.8 *MPa* at 298 *K*, which is in accordance with the result in the work by Ihm et al. [19]. One can also find that the lower the temperature, the excess point of the 8 and 9 Å systems appears at more lower pressure. Our estimated uptake rates are all above 30% higher than Ihm's [19]. The data in Fig. 6 can also be found in Table 1. In order to compare with the experimental results presented in the work Gallego et al. [52], we calculate the system with 9 Å separation at 298 *K* and 5, 21 *MPa*. The average H_2 density at 298 *K* and 5 *MPa* is around 0.024 $mol \cdot cm^{-3}$, which is very close to the experimental value 0.027 $mol \cdot cm^{-3}$ [52]. At 298 *K* and 21 *MPa*, our estimated uptake rate is 3.65 *wt.*% for the 9 Å system with a deviation of ~9% compared with the experimental result [52].

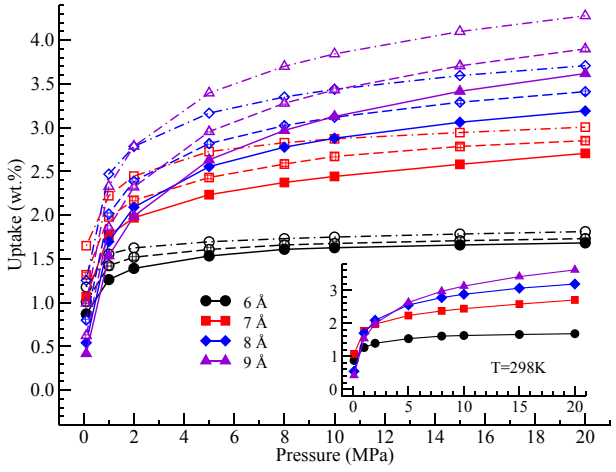

Fig. 6 – The dependency of the hydrogen uptake rates of the bilayer graphene system on the pressure, temperature and interlayer distance. The systems with 6, 7, 8 and 9 Å separations are indicated by circle, diamond, square, and triangle, respectively. The solid lines (with solid symbols), dashed lines (with patterned symbols) and dot-dashed lines (with hollow symbols) show the results at three different temperatures 298, 273, 243 *K*. The inset represents the picked up results of the systems at 298 *K* as an example to clarify the dependency.

Conclusion

The VE method has been used to investigate the fugacity coefficients of the hydrogen fluid as a function of the temperature and pressure. The second and third virial coefficients have been determined based on the simple LJ- and FH-potential models. The FH-potential can describe the fugacity more accurate than the simple LJ-potential because of its additional quantum correction term. To improve the calculated fugacity coefficients, the fourth virial term has also been involved in our calculation on the basis of a $n = 24$ soft sphere potential model. Until the fourth order can the VE provide a desirable results. More importantly, the results from our VE method have full physical meanings. Via the equilibrium of the chemical potentials between the in- and outside phases of the hydrogen fluid as well as the definition of the fugacity, we have re-assessed the hydrogen storage capacity of the expanded bilayer graphene sheets on the basis of our calculated fugacity coefficients and the EOS. The bilayer graphene sheets with an 9 Å interlayer distance possess the relatively high hydrogen uptake rates, which are around 3.84 *wt.*% and 3.65 *wt.*% at $T = 243$ *K*, $P = 10$ *MPa* and $T = 298$ *K*, $P = 21$ *MPa* with B3LYP-D2 method, respectively. These results agree very well with the experimental data contributed by Gallego et al. [52]. Compared to the research by Ihm and his co-workers [19], our results are accurate and reasonable. It has been proved that our VE method can be used in predicting the hydrogen storage capacity. We believe that our VE method also has the vigorous potential for the predictions of the storage capacities or the select capabilities in certain material system for

Table 1 – The uptake rates of four expanded bilayer graphene systems with the interlayer distances of 6, 7, 8 and 9 Å under three typical temperatures and several appropriate pressures.

P [MPa]		0.1	1.0	2.0	5.0	8.0	10.0	15.0	20.0	
6 Å	243 K	1.18	1.55	1.62	1.70	1.73	1.75	1.78	1.81	wt.%
	273 K	1.01	1.42	1.52	1.61	1.66	1.68	1.71	1.73	
	298 K	0.87	1.26	1.39	1.53	1.61	1.63	1.66	1.68	
7 Å	243 K	1.65	2.22	2.45	2.73	2.83	2.87	2.94	3.01	
	273 K	1.32	1.98	2.17	2.43	2.58	2.67	2.78	2.85	
	298 K	1.07	1.77	1.97	2.23	2.37	2.44	2.58	2.71	
8 Å	243 K	1.25	2.47	2.78	3.17	3.35	3.44	3.60	3.71	
	273 K	0.80	2.01	2.39	2.82	3.02	3.12	3.29	3.41	
	298 K	0.54	1.70	2.09	2.55	2.78	2.88	3.06	3.19	
9 Å	243 K	0.99	2.33	2.79	3.40	3.70	3.84	4.10	4.28	
	273 K	0.62	1.86	2.32	2.95	3.28	3.43	3.71	3.90	
	298 K	0.42	1.53	1.99	2.63	2.97	3.13	3.42	3.62	

other non-polar particle fluids, e.g., noble gases, methane, nitrogen, oxygen and so on.

Acknowledgments

This work is supported by National Natural Science Foundation of China (Grant No. 21173096).

Appendix A. Supplementary data

Supplementary data related to this article can be found at http://dx.doi.org/10.1016/j.ijhydene.2015.07.005.

REFERENCES

[1] Bhatia SK, Myers AL. Optimum conditions for adsorptive storage. Langmuir 2006;22:1688.
[2] Wang Q, Sun Q, Jena P, Kawazoe Y. Potential of AlN nanostructures as hydrogen storage materials. ACS Nano 2009;3:621.
[3] Jena P. Materials for hydrogen storage: past, present, and future. J Phys Chem Lett 2011;2:206.
[4] Colón YJ, Fairen-Jimenez D, Wilmer CE, Snurr RQ. High-throughput screening of porous crystalline materials for hydrogen storage capacity near room temperature. J Phys Chem C 2014;118:5383.
[5] Zhao G, Li Y, Liu C, Wang Y, Sun J, Gu Y, et al. Boron nitride substrate-induced reversible hydrogen storage in bilayer solid matrix via interlayer spacing. Int J Hydrogen Energy 2012;37:9677.
[6] Avdeenkov AV, Bodrenko IV, Bessarabov DG, Bibikov AV, Nikolaev AV, Taran MD, et al. Thermodynamical model for hydrogen storage capacity in carbon nanostructures. Int J Hydrogen Energy 2015;40:4184.
[7] Lu J, Guo Y, Zhang Y, Cao J. Li decorated 6,6,12-graphyne: a new star for hydrogen storage material. Int J Hydrogen Energy 2014;39:17112.
[8] Guo Y, Lan X, Cao J, Xu B, Xia Y, Yin J, et al. A comparative study of the reversible hydrogen storage behavior in several metal decorated graphyne. Int J Hydrogen Energy 2013;38:3987.
[9] Tylianakis E, Dimitrakakis GK, Martin-Martinez FJ, Melchor S. Designing novel nanoporous architectures of carbon nanotubes for hydrogen storage. Int J Hydrogen Energy 2014;39:9825.
[10] Ao Z, Dou S, Xu Z, Jiang Q, Wang G. Hydrogen storage in porous graphene with Al decoration. Int J Hydrogen Energy 2014;39:16244.
[11] Yadav S, Tam J, Singh CV. A first principles study of hydrogen storage on lithium decorated two dimensional carbon allotropes. Int J Hydrogen Energy 2015;40:6128.
[12] Mahdizadeh SJ, Goharshadi EK. Hydrogen storage on silicon, carbon, and silicon carbide nanotubes: a combined quantum mechanics and grand canonical Monte Carlo simulation study. Int J Hydrogen Energy 2014;39:1719.
[13] Grimme S. Semiempirical GGA-type density functional constructed with a long-range dispersion correction. J Comput Chem 2006;27:1787.
[14] Tkatchenko A, Scheffler M. Accurate molecular van der Waals interactions from ground-state electron density and free-atom reference data. Phys Rev Lett 2009;102:073005.
[15] Ortmann F, Bechstedt F, Schmidt WG. Semiempirical van der Waals correction to the density functional description of solids and molecular structures. Phys Rev B 2006;73:205101.
[16] Car R, Parrinello M. Unified approach for molecular dynamics and density-functional theory. Phys Rev Lett 1985;55:2471.
[17] Peng LJ, Morris JR. Prediction of hydrogen adsorption properties in expanded graphite model and in nanoporous carbon. J Phys Chem C 2010;114:15522.
[18] Peng LJ, Morris JR. Structure and hydrogen adsorption properties of low density nanoporous carbons from simulations. Carbon 2012;50:1394.
[19] Ihm Y, Cooper VR, Peng L, Morris JR. The influence of dispersion interactions on the hydrogen adsorption properties of expanded graphite. J Phys Condens Matter 2012;24:424205.
[20] Ihm Y, Cooper VR, Gallego NC, Contescu CI, Morris JR. Microstructure-dependent gas adsorption: accurate predictions of methane uptake in nanoporous carbons. J Chem Theory Comput 2014;10:1–4.
[21] Patchkovskii S, Tse JS, Yurchenko SN, Zhechkov L, Heine T, Seifert G. Graphene nanostructures as tunable storage media for molecular hydrogen. Proc Natl Acad Sci 2005;102:10439.
[22] Cabria I, López MJ, Alonso JA. Hydrogen storage capacities of nanoporous carbon calculated by density functional and Moller-Plesset methods. Phys Rev B 2008;78:075415.
[23] Shaw HR, Wones DR. Fugacity coefficients for hydrogen gas between 0 and 1000 C, for pressures to 3000 atm. Am J Sci 1964;262:918.
[24] Mills RL, Liebenberg DH, Bronson JC, Schmidt LC. Equation of state of fluid n-H_2 from P-V-T and sound velocity measurements to 20 kbar. J Chem Phys 1977;66:3076.

[25] Setzmann U, Wagner W. A new equation of state and tables of thermodynamic properties for methane covering the range from the melting line to 625 K at pressures up to 100 MPa. J Phys Chem Ref Data 1991;20:1061.
[26] Hirschfelder TO, Curtiss Ch F, Bird RB. Molecular theory of gases and liquids. New York: John Wiley and Sons, Inc; 1954.
[27] Feynman RP, Hibbs A. Quantum mechanics and path-integrals. New York: McGraw-Hill; 1965.
[28] Guillot B, Guissani Y. Quantum effects in simulated water by the Feynman-Hibbs approach. J Chem Phys 1998;108:10162.
[29] Levesque D, Gicquel A, Darkrim FL, Kayiran SB. Monte Carlo simulations of hydrogen storage in carbon nanotubes. J Phys Cond Matter 2002;14:9285.
[30] Darkrim F, Levesque D. Monte Carlo simulations of hydrogen adsorption in single-walled carbon nanotubes. J Chem Phys 1998;109:4981.
[31] Cheng J, Zhang L, Ding R, Ding Z, Wang X, Wang Z. Grand canonical Monte Carlo simulation of hydrogen physisorption in single-walled boron nitride nanotubes. Int J Hydrogen Energy 2007;32:3402.
[32] Dimitrakakis GK, Tylianakis E, Froudakis GE. Pillared graphene: a new 3-D network nanostructure for enhanced hydrogen storage. Nano Lett 2008;8:3166.
[33] Leachman JW, Jacobsen RT, Penoncello SG, Lemmon EW. Fundamental equations of state for parahydrogen, normal hydrogen, and orthohydrogen. J Phys Chem Ref Data 2009;38:721.
[34] Stockmayer WH. Second virial coefficients of polar gases. J Chem Phys 1941;9:398.
[35] Bartke J, Hentschke R. Phase behavior of the Stockmayer fluid via molecular dynamics simulation. Phys Rev E 2007;75:061503.
[36] Patkowski K, Cencek W, Jankowski P, Szalewicz K, Mehl JB, Garberoglio G, et al. Potential energy surface for interactions between two hydrogen molecules. J Chem Phys 2008;129:094304.
[37] Garberoglio G, Jankowski P, Szalewicz K, Harvey AH. Second virial coefficients of H_2 and its isotopologues from a six-dimensional potential. J Chem Phys 2012;137:154308.
[38] Kusalik PG, Liden F, Svishchev IM. Calculation of the third virial coefficient for water. J Chem Phys 1995;103:10169.
[39] Garberoglio G. On the contribution of non-additive three-body interactions to the third virial coefficient of para-hydrogen. Chem Phys Lett 2013;557:26.
[40] Axilrod BM, Teller E. Interaction of the van der Waals type between three atoms. J Chem Phys 1943;11:299.
[41] Muto Y. The force between nonpolar molecules. Proc Phys Math Soc Jpn 1943;17:629.
[42] Manzhos S, Nakai K, Yamashita K. Three-body interactions in clusters COC(pH2)n. Chem Phys Lett 2010;493:229.
[43] Barlow NS, Schultz AJ, Weinstein SJ, Kofke DA. An asymptotically consistent approximant method with application to soft- and hard-sphere fluids. J Chem Phys 2012;137:204102.
[44] Wheatley RJ. Inverse power potentials: virial coefficients and a general equation of state. J Phys Chem B 2005;109:7463.
[45] Tan TB, Schultz AJ, Kofke DA. Virial coefficients, equation of state, and solid fluid coexistence for the soft sphere model. Mol Phys 2011;109:123.
[46] Clisby N, McCoy BM. Ninth and tenth order virial coefficients for hard spheres in D dimensions. J Stat Phys 2006;122:15.
[47] Younglove BA. Thermophysical properties of fluids. I. Argon, ethylene, parahydrogen, nitrogen, nitrogen trifluoride, and oxygen. J Phys Chem Ref Data 1982;14:619.
[48] Dovesi R, Saunders VR, Roetti C, Orlando R, Zicovich-Wilson CM, Pascale F, et al. CRYSTAL14 user's manual. Torino: University of Torino; 1943. Dovesi R, Orlando R, Erba A, Zicovich-Wilson CM, Civalleri B, Casassa S, et al. CRYSTAL14: a program for the ab initio investigation of crystalline solids. Int. J. Quantum Chem 2004;11:299.
[49] Peintinger MF, Vilela Oliveira D, Bredow T. Consistent Gaussian basis sets of triple-zeta valence with polarization quality for solid-state calculations. J Comput Chem 2013;34:451.
[50] Monkhorst HJ, Pack JD. Semiempirical van der Waals correction to the density functional description of solids and molecular structures. Phys Rev B 1976;13:5188.
[51] Anthony JW, Bideaux RA, Bladh KW, Nichols MC. Handbook of mineralogy. Elements, sulfides, sulfosalts, vol. I. Tucson, Arizona: Mineral Data Publishing; 1990.
[52] Gallego NC, He L, Saha D, Contescu CI, Melnichenko YB. Semiempirical van der Waals correction to the density functional description of solids and molecular structures. J Am Chem Soc 2011;133:13794.